SCIENTIFIC REPORTS

OPEN

SUBJECT AREAS:
FUEL CELLS
NANOPARTICLES

Received
28 March 2014

Accepted
15 May 2014

Published
3 June 2014

Correspondence and requests for materials should be addressed to K.X. (xiekui@hfut.edu.cn) or Y.C.W. (ycwu@hfut.edu.cn)

# *In situ* Growth of $Ni_xCu_{1-x}$ Alloy Nanocatalysts on Redox-reversible Rutile $(Nb,Ti)O_4$ Towards High-Temperature Carbon Dioxide Electrolysis

Haoshan Wei[1], Kui Xie[1,2], Jun Zhang[1], Yong Zhang[1,2], Yan Wang[1,2], Yongqiang Qin[1], Jiewu Cui[1], Jian Yan[1,2] & Yucheng Wu[1,2]

[1]Department of Energy Materials, School of Materials Science and Engineering, Hefei University of Technology, No.193 Tunxi Road, Hefei, Anhui 230009, China, [2]Key Laboratory of Advanced Functional Materials and Devices, Hefei University of Technology, No.193 Tunxi Road, Hefei, Anhui 230009, China.

**In this paper, we report the *in situ* growth of $Ni_xCu_{1-x}$ (x = 0, 0.25, 0.50, 0.75 and 1.0) alloy catalysts to anchor and decorate a redox-reversible $Nb_{1.33}Ti_{0.67}O_4$ ceramic substrate with the aim of tailoring the electrocatalytic activity of the composite materials through direct exsolution of metal particles from the crystal lattice of a ceramic oxide in a reducing atmosphere at high temperatures. Combined analysis using XRD, SEM, EDS, TGA, TEM and XPS confirmed the completely reversible exsolution/dissolution of the $Ni_xCu_{1-x}$ alloy particles during the redox cycling treatments. TEM results revealed that the alloy particles were exsolved to anchor onto the surface of highly electronically conducting $Nb_{1.33}Ti_{0.67}O_4$ in the form of heterojunctions. The electrical properties of the nanosized $Ni_xCu_{1-x}/Nb_{1.33}Ti_{0.67}O_4$ were systematically investigated and correlated to the electrochemical performance of the composite electrodes. A strong dependence of the improved electrode activity on the alloy compositions was observed in reducing atmospheres at high temperatures. Direct electrolysis of $CO_2$ at the $Ni_xCu_{1-x}/Nb_{1.33}Ti_{0.67}O_4$ composite cathodes was investigated in solid-oxide electrolysers. The $CO_2$ splitting rates were observed to be positively correlated with the Ni composition; however, the $Ni_{0.75}Cu_{0.25}$ combined the advantages of metallic nickel and copper and therefore maximised the current efficiencies.**

Solid oxide electrolysers have demonstrated the tremendous advantages of electrochemical conversion of $CO_2$ into fuels with high efficiencies using renewable electrical energy[1–3]. Oxide-ion-conducting solid oxide electrolysers can directly electrolyse $CO_2$ into CO and pure oxygen under external applied potentials. At the cathode, $CO_2$ molecules are electrochemically split into CO while the generated $O^{2-}$ ions are transported through the electrolyte membrane to the anode compartment where pure $O_2$ gas is formed and released[4,5].

The conventional Ni/YSZ electrode has exhibited excellent steam-electrolysis performance under a reducing atmosphere; however, the Ni-cermets are not redox stable and require a significant concentration of reducing gas flowing over the Ni metal to avoid the oxidation of Ni to NiO[6,7]. Similarly, the flowing of CO to the composite electrode is also necessary during electrolysis of $CO_2$ because the oxidation of Ni occurs at high temperatures[8]. Furthermore, the catalytic activity of Ni metal toward the splitting of $CO_2$ is relatively high; carbon deposition most likely occurs and results in the degradation of cell performance. Some researchers have demonstrated that the deposition of carbon is likely caused by reactions that occur over the catalyst and favour to occur only when CO is present in the chemical reaction system[8–10]. Cu/YSZ and Cu/SDC have also been considered as potential electrodes because of their ability to adsorb $CO_2$, resistance to carbon fouling and low cost; however, the catalytic activity of Cu toward $CO_2$ splitting is inferior to that of Ni[11,12]. Cu similarly oxidises during the direct electrolysis of $CO_2$ or $H_2O$ in the absence of a reducing gas flowing over the composite cathode at high temperatures.

High-temperature electrolysis based on the redox-stable LSCM or LSTO cathode has been reported for the direct electrolysis of $H_2O$, $CO_2$ or $H_2O/CO_2$, and promising electrode performances have also been observed[13–17]. However, the LSCM, as a p-type conductor, is not well adapted to strong reducing potentials. LSCM exhibits lower conductivity than other cathode materials and undergoes adverse chemical changes under such extreme conditions; these changes lead to a large electrode polarisation resistance and to degradation of the electrolysis

performance[18,19]. Direct electrolysis of $CO_2$ with a current efficiency as high as approximately 50–60% has been achieved with LSCM cathodes, as reported in our previous work; however, rapid electrode degradation occurs at an external load of 2 V at 800°C[14]. By contrast, LSTO, which exhibits n-type conductivity upon reduction, has been considered a breakthrough in the development of redox-stable anode materials for SOFCs and has also been utilised for direct high-temperature electrolysis[20]. However, this material's insufficient catalytic activity still restricts the electrode polarisation and current efficiency during high-temperature electrolysis[15]. To improve the performance of LSTO, metal catalysts have been introduced, which has resulted in a substantially enhanced electrode performance[21,22]. However, control of the morphology of such catalysts on the substrate is difficult, and operation over a long period of time would risk catalyst agglomeration and, therefore, performance degradation. As documented in our previous work[16,23–24], steam electrolysis based on Ni- or Fe-impregnated LSCM or LSTO is stable during the first hour of operation at a load of 1.5–2 V, whereas an approximately 20–30% degradation in cell performance is observed when the operating time exceeds 5 h because of the agglomeration of metal nanoparticles on the surface of the composite cathode skeleton.

An alternative method is to incorporate the catalyst as a dopant within a host lattice during the synthesis of the catalyst in air, which is then exsolved at the surface in the form of catalytically active metallic nanoparticles or microparticles under reducing conditions[25]. Upon re-oxidation, the dopant can be re-incorporated into the host lattice, yielding a regenerative catalyst. In this case, any possible agglomeration of exsolved metallic nanoparticles on the substrate surface can be avoided by periodically exposing the material to oxidising conditions. Fluorite oxide, $NbTi_{0.5}Ni_{0.5}O_4$ (NTNO), which is a single-phase rutile-type structure with the tetragonal ($P4_2/mnm$) space group, was first reported as a potential anode material for solid oxide fuel cells by Irvine et al.[26,27]. Nanoparticles of metallic Ni can be exsolved at the surface of the highly-conducting $Nb_{1.33}Ti_{0.67}O_4$ substrate after high-temperature reduction under a reducing gas. The $Nb_{1.33}Ti_{0.67}O_4$ is a mixed conductor because of the edge sharing of $NbO_6$ octahedra along the c-axis, which result in Nb–Nb metal bond overlap with an inter-metallic distance of 3 Å. This high electronic conductivity is facilitated by the edge-sharing octahedra along the c-axis[28]. In our previous work, the nanosized $Ni/Nb_{1.33}Ti_{0.67}O_4$ composite exhibited promising electrode polarisations and current efficiencies for the direct steam electrolysis[29].

Copper-based catalysts exhibit lower selectivity toward $H_2$ than toward CO or $CO_2$ because of their high over-potential of hydrogen evolution[42]; however, their excellent $CO_2$/monoxide adsorption properties and resistance to carbon fouling make copper-based catalysts appealing to many researchers[30–33]. In contrast to copper, Ni metal exhibits high catalytic activity but probably tends to be prone to high coke formation; such a severe deactivation poses a serious obstacle to the future application of Ni-metal catalysts. Coke is favour to occur when CO and hydrocarbons are present for their chemisorption[34]. Some researchers have taken a compromise approach by mechanically mixing Ni and Cu particles to form a Ni + Cu composite and therefore utilise the respective catalysis characteristics of both nickel and copper[35–38]. The performance trends reported for electrodes prepared by impregnation and those prepared by mechanical alloying are similar; mechanical alloying is therefore a promising route to prepare electrode materials. Recently, a novel NiCu alloy catalyst was reported, and its catalytic behaviour can be continuously tuned by tailoring the molar ratio between Cu and Ni in the alloy[39,40]. Xie et al. observed that the 50%Ni-50%Cu alloy exhibits excellent catalytic performance for $CH_4$ dissociation through theoretical first-principles calculations[41]. Bujalski and co-workers demonstrated the tailored catalytic activity of the 50%Ni-50%Cu alloy for hydrogen production from the partial oxidation of methane and methanol[42]. The NiCu alloy catalyst exhibits the advantages of both metallic nickel and metallic copper. Furthermore, the synergistic effect makes the NiCu alloy with continuously tuned compositions an outstanding catalyst in many scientific fields[43–45].

Here, we report the reversible *in situ* growth of $Ni_xCu_{1-x}$ (x = 0, 0.25, 0.50, 0.75 and 1.0) alloy catalysts to anchor and decorate the redox-reversible $Nb_{1.33}Ti_{0.67}O_4$ ceramic substrate with the aim of tailoring the electrocatalytic activity of the composite materials through direct exsolution of metal particles from the crystal lattice of the ceramic oxide. The anchored interface is expected to enhance the electrocatalytic kinetics and the high-temperature stability of such nanoparticles. The electrical properties of the ceramic composite are investigated and further correlated to the electrochemical performance of their composite electrodes. Direct electrolysis of $CO_2$ is then performed using the $Ni_xCu_{1-x}/Nb_{1.33}Ti_{0.67}O_4$ composite cathode in a solid-oxide electrolyser at high temperatures.

## Methods

All the powders were purchased from SINOPHARM Chemical Reagent Co., Ltd (China) unless specified otherwise. The synthesis of $NbTi_{0.5}(Ni_xCu_{1-x})_{0.5}O_4$ (x = 1.0, NTNO; x = 0.75, $NTN_3C_1O$; x = 0.5, $NTN_1C_1O$; x = 0.25, $NTN_1C_3O$; x = 0, NTCO) was carried out by a solid-state reaction using an appropriate mixture of $Nb_2O_5$, $TiO_2$, CuO and NiO powders[29]. The mixture was ball-milled in acetone, dried, pressed into pellets at room temperature and treated at 1300, 1150, 1100, 1050 and 1000°C for the NTNO, $NTN_3C_1O$, $NTN_1C_1O$, $NTN_1C_3O$ and NTCO, respectively, for 20 h in air. The $(La_{0.8}Sr_{0.2})_{0.95}MnO_{3-\delta}$ (LSM) was synthesised via the combustion method using $La_2O_3$, $SrCO_3$ and $C_4H_6MnO_4{\cdot}4H_2O$ as precursors; the final heat treatment was conducted at 1100°C for 3 h in air. However, the $Ce_{0.8}Sm_{0.2}O_{2-\delta}$ (SDC) powders were prepared using the aforementioned method with $Sm_2O_3$ and $Ce(NO_3)_4{\cdot}6H_2O$ precursors followed by a treatment at 800°C for 3 h in air[52,53]. The NTNO, $NTN_3C_1O$, $NTN_1C_1O$, $NTN_1C_3O$ and NTCO samples were sintered and then reduced (5% $H_2$/Ar) at 1300, 1250, 1150, 1050 and 1000°C (3°C $min^{-1}$), respectively, for 20 h to achieve the reduced form of the composite $Nb_{1.33}Ti_{0.67}O_4$ + $Ni_xCu_{1-x}$. The *in situ* growth of $Ni_xCu_{1-x}$ alloy nanocatalysts when all of the oxide forms were reduced in reducing atmosphere (5% $H_2$/Ar) at 1050°C (3°C $min^{-1}$) for approximately 20 h. The reduction-oxidation cycles of the composite materials were conducted for another three cycles under reducing or oxidising atmospheres (5% $H_2$/Ar or static air).

The X-ray diffraction (XRD, 2θ = 3°·$min^{-1}$, 2θ = 10–90°, D/MAX2500V, Rigaku Corporation, Japan) analyses were performed to characterise the structural changes of the materials after the redox cycles. The microstructure of the $NbTi_{0.5}(Ni_xCu_{1-x})_{0.5}O_4$ and $Ni_xCu_{1-x}/Nb_{1.33}Ti_{0.67}O_4$ were investigated by scanning electron microscopy (SEM, SU8020, HITACHI, Ltd., Japan) coupled with energy-dispersive X-ray spectroscopy (EDS). The valence states of the elements in the $NbTi_{0.5}(Ni_xCu_{1-x})_{0.5}O_4$ and $Ni_xCu_{1-x}/Nb_{1.33}Ti_{0.67}O_4$ were analysed using an ESCALAB250 spectrometer equipped with an Al Kα (1486.6 eV) radiation source. The thermogravimetric analysis (TGA, STA449F3, Germany) of the oxidised NTNO and $NTN_1C_1O$ samples was conducted from room temperature to 1000°C and then back to room temperature under a reducing atmosphere; the heating rate was 4°C $min^{-1}$, and the flow rate of 5% $H_2$/Ar (99.99% purity). Transmission electron microscopy (TEM) analysis with selected-area diffraction was performed to observe the oxidised and reduced $NTN_1C_1O$ powders; the analyses were performed on a JEOL 2100F field-emission transmission electron microscope operated at 200 kV.

Approximately 2.0 g of NTNO, $NTN_3C_1O$, $NTN_1C_1O$, $NTN_1C_3O$ or NTCO powder was compacted into a bar at a pressure of 6 MPa (20.0 mm × 7.0 mm × 2.4 mm) and subsequently sintered at 1300, 1150, 1100, 1050 or 1000°C for 10 h, respectively. The relative densities of all the samples were similar to each other, at approximately 80%. The bars were reduced completely at 1300, 1150, 1100, 1050 or 1000°C, respectively, for 20 h in a reducing atmosphere (5% $H_2$/Ar) for the conductivity tests. The conductivity of the reduced samples, $Ni_xCu_{1-x}/Nb_{1.33}Ti_{0.67}O_4$, were tested in 5% $H_2$/Ar (99.99% purity) from room temperature to 800°C using the DC four-terminal method; the conductivity was recorded at a step of 0.5°C using an online system. The dependence of the conductivity on the oxygen partial pressure was tested at 800°C under an oxygen partial pressure that ranged from $10^{-2}$ to $10^{-19}$ atm; the oxygen partial pressure was adjusted by variation of the flow rate of the dry 5% $H_2$/Ar. The oxygen partial pressure ($lgpO_2$) and the conductivities were recorded using an online oxygen sensor (1231, $ZrO_2$-based oxygen sensor, Noveltech, Australia) and an online multimeter (Keithley 2000 digital multimeter, Keithley Instruments, Inc., USA), respectively.

We prepared the 1 mm-thick YSZ disc electrolyte supports by dry-pressing the YSZ powder into green disks with a diameter of 20 mm and subsequently sintering the disks at 1500°C (2°C·$min^{-1}$) for 10 h in air. The two surfaces of the obtained YSZ electrolyte support were mechanically polished and then ultrasonically cleaned in distilled water. The $NbTi_{0.5}(Ni_xCu_{1-x})_{0.5}O_4$-SDC composite electrode slurries were prepared by milling the SDC powder with $NbTi_{0.5}(Ni_xCu_{1-x})_{0.5}O_4$ powder at a 35 : 65 weight ratio in alpha-terpineol with cellulose as an additive[54,55]. The electrode slurries were then coated onto the electrolyte in symmetric positions in an area of 1 $cm^2$ to assemble the symmetric cells; the cells were subsequently subjected to a heat treat-

ment at 1000°C (3°C $min^{-1}$) for 3 h in air. The current-collection layer was prepared using silver paste (SS-8060, Xinluyi, Shanghai, China), which was printed onto both electrode surfaces. The external circuit was constructed using silver electrical wire (0.1 mm in diameter), which was then connected to both current collectors using silver paste (DAD87, Shanghai Research Institute for Synthetic Resins) followed by firing at 550°C (3°C $min^{-1}$) for 30 min in air. The AC impedance of the symmetric solid-oxide cells was tested at 800°C with the two electrodes exposed to different hydrogen partial pressures at the open-circuit voltage (OCV) using an electrochemical station (IM6, Zahner, Germany) with a frequency range of 4 M–0.1 Hz and a current strength of 10 mA in two-electrode mode. The electrode polarisation resistance was calculated by modelling the spectra using the Zview software. The gas flow rate was controlled at 20 ml $min^{-1}$ using a mass flow meter (D08-3F, Sevenstar, China) to mix different ratios of $H_2$ (99.99%) and $N_2$ (99.99%).

The solid-oxide electrolysers were constructed using $NbTi_{0.5}(Ni_xCu_{1-x})_{0.5}O_4$ as the cathode and LSM as the anode, with YSZ as the electrolyte. The two surfaces of the electrolyte were coated with $NbTi_{0.5}(Ni_xCu_{1-x})_{0.5}O_4$-SDC slurry and LSM-SDC slurry in symmetric positions with an area of 1 $cm^2$ and were subsequently subjected to the same heat treatment used for the symmetric solid-oxide cells, as previously described. The single solid-oxide electrolyser was sealed in a home-made testing jig using ceramic paste (JD-767, Jiudian, Dongguan, China) for the electrochemical measurements. The electrochemical measurements, including the AC impedance and current–voltage (I–V) plots of the solid oxide electrolyser, were performed with the cathode electrode exposed to flowing pure $CO_2$ (99.99% in purity) and the oxygen electrode in static air at 800°C. The electrolysis of $CO_2$ was performed at different applied voltages with $CO_2$ fed into the cathode at 800°C. The output gas from the cathode was analysed using an online gas chromatograph (GC9790II, Fuli, Zhejiang, China) to determine the concentration of CO.

## Results and Discussion

Fig. 1 (a) shows the XRD patterns of the single-phase rutile-type $NbTi_{0.5}(Ni_xCu_{1-x})_{0.5}O_4$ (x = 1, 0.75, 0.5, 0.25, 0), which confirms the homogeneous solid solution, i.e., even the composition of Ni and Cu changes in a wide range. The structures of the $NbTi_{0.5}(Ni_xCu_{1-x})_{0.5}O_4$ are tetragonal with the *P4₂/mnm* space group[29]. Fig. 2 shows the parameters for $NbTi_{0.5}(Ni_xCu_{1-x})_{0.5}O_4$ (x = 1, 0.75, 0.5, 0.25, 0) calculated from the XRD data. We observed that the cell parameters a and c increase from 4.6944(8) Å and 3.0229(5) Å to 4.6974(8) Å and 3.0297(4) Å when the proportion of nickel is decreased from 1 to 0.5, respectively. However, a remarkable decrease of cell parameter a occurs, whereas the cell parameter c sharply increases from 3.0297(4) Å to 3.0378(7) Å and then decreases to 3.0316(2) Å when the Ni proportion, x, is decreased to 0. Notably, the cell volumes are distributed as a pyramid with the cell volume of x = 0 and 1 at the bottom, which may be related to the larger ionic radii of $Ni^{2+}$ (0.69 Å) and $Cu^{2+}$ (0.73 Å) compared with that of $Ti^{4+}$ (0.605 Å) with the same coordination numbers. The incorporation of $Cu^{2+}$ may play a leading role in the expansion of the cell parameters, especially the c-axis parameter, possibly because of an increase in lattice strength with Cu doping. Fig. 1 (b) shows the XRD patterns of reduced $NbTi_{0.5}(Ni_xCu_{1-x})_{0.5}O_4$ (x = 1, 0.75, 0.5, 0.25, 0), which confirms that the reduced $NbTi_{0.5}(Ni_xCu_{1-x})_{0.5}O_4$ are a mixture of two phases: $Ni_xCu_{1-x}$ + $Nb_{1.33}Ti_{0.67}O_4$. As shown in Fig. 1 (b), the $NbTi_{0.5}(Ni_xCu_{1-x})_{0.5}O_4$ changes into $Nb_{1.33}Ti_{0.67}O_4$ (PDF No. 053-0293) and metallic $Ni_xCu_{1-x}$ alloy upon high-temperature reduction in 5% $H_2$/Ar (99.99%). This result confirms the phase change of $NbTi_{0.5}(Ni_xCu_{1-x})_{0.5}O_4$ to highly electrically conducting $Nb_{1.33}Ti_{0.67}O_4$ and pure catalytically active metallic $Ni_xCu_{1-x}$ alloy.

To investigate the reversibility of the exsolution of the metallic $Ni_xCu_{1-x}$, the composite powders were further treated for another three redox cycles at 1050°C under a reducing atmosphere (5% $H_2$/Ar) and a oxidising atmosphere (static air) for 20 h. Fig. 1 (c) shows the XRD patterns of the composite after oxidation, which again confirms the successful integration of $Ni_xCu_{1-x}$ alloys into the $Nb_{1.33}Ti_{0.67}O_4$ substrate and the formation of a single-phase $NbTi_{0.5}(Ni_xCu_{1-x})_{0.5}O_4$ solid solution. No phase impurities are observed in the case of $NbTi_{0.5}(Ni_xCu_{1-x})_{0.5}O_4$, thereby firmly verifying the superior redox reversibility of the $NbTi_{0.5}(Ni_xCu_{1-x})_{0.5}O_4$ ceramics. As shown in Fig. 1 (d), the corresponding XRD patterns confirm that the reduced $NbTi_{0.5}(Ni_xCu_{1-x})_{0.5}O_4$ (x = 1, 0.75, 0.5, 0.25, 0) are still composed of conducting ceramic $Nb_{1.33}Ti_{0.67}O_4$ and metallic alloy powders, which further demonstrates the excellent reversible exsolution of the metallic $Ni_xCu_{1-x}$ from the lattice of $NbTi_{0.5}(Ni_xCu_{1-x})_{0.5}O_4$ through a reversible phase transition. The three successive redox treatment cycles of $NbTi_{0.5}(Ni_xCu_{1-x})_{0.5}O_4$ solid solutions suggest that the parent material $NbTi_{0.5}(Ni_xCu_{1-x})_{0.5}O_4$ and the $Ni_xCu_{1-x}$ + $Nb_{1.33}Ti_{0.67}O_4$ composite materials exhibit excellent redox reversibility. The metallic $Ni_xCu_{1-x}$ alloys can be repeatedly exsolved from the $NbTi_{0.5}(Ni_xCu_{1-x})_{0.5}O_4$ after the reduction and again integrated back into the $Nb_{1.33}Ti_{0.67}O_4$ substrate to form a homogeneous phase.

To further validate the elemental valence change in redox cycles of the $NbTi_{0.5}(Ni_xCu_{1-x})_{0.5}O_4$ solid solution, we performed XPS on the oxidised and reduced $NTN_3C_1O$ ($NbTi_{0.5}(Ni_{0.75}Cu_{0.25})_{0.5}O_4$ and $Ni_{0.75}Cu_{0.25}$ + $Nb_{1.33}Ti_{0.67}O_4$) samples. All XPS patterns were fitted using a Shirley-type background subtraction method. The background functions for different the spectra of different elements were fitted using 80% Gaussian and 20% Lorentzian functions[46]. As shown in Fig. 3 (a), only $Nb^{5+}$ is observed in the oxidised $NTN_3C_1O$ sample; however, the $Nb^{5+}$ is reduced to $Nb^{4+}$ in the $Nb_{1.33}Ti_{0.67}O_4$ substrate when the sample is treated under a reducing atmosphere at 1200°C for 20 h, as seen in Fig. 3 (b)[28,47]. The low valence of the $Nb^{4+}$ ions favours the formation of Nb-Nb metal bonds, and the electronic conductivity is thus highly facilitated, resulting in enhanced electrical conductivity of $Nb_{1.33}Ti_{0.67}O_4$. By contrast, element Ti, as exhibited in Fig. 3 (c), is completely in the $Ti^{4+}$ state in the oxidised $NTN_3C_1O$ sample; however, the low-valence $Ti^{3+}$ is also observed in the reduced sample, $Nb_{1.33}Ti_{0.67}O_4$ + $Ni_{0.5}Cu_{0.5}$, as shown in Fig. 3 (d), due to the chemical reduction of $Ti^{4+}$ to $Ti^{3+}$ after the heat treatment under a reducing atmosphere. We reasonably speculated that the $Nb_{1.33}Ti_{0.67}O_4$ is actually oxygen-deficient $Nb_{1.33}Ti_{0.67}O_{4-\delta}$ according to the charge balance[29]. The $Ti^{3+}$ (2p1/2) and $Ti^{3+}$ (2p3/2) peaks are observed at 462.80 eV and 457.80 eV, respectively, whereas the $Ti^{4+}$ (2p1/2) and $Ti^{4+}$ (2p3/2) show peaks at 464.80 eV and 458.10 eV, respectively[29]. Furthermore, the low-valence $Ti^{3+}$ represents an approximately 0.174 mole ratio of all of the Ti according to this result, which indicates an oxygen deficiency of $\delta$ = 0.058 and a chemical formula of $Nb_{1.33}Ti_{0.67}O_{3.942}$. The Ni and Cu in the $NTN_1C_1O$ are in the form of $Ni^{2+}$ and $Cu^{2+}$, as shown in Fig. 3 (e) and Fig. 3 (g), respectively. In Fig. 3 (f), the $Ni^0$ (2p1/2) peaks are observed at 873.86 and 869.40 eV, whereas the $Ni^0$ (2p3/2) has three peaks at 861.0, 869.40 and 852.0 eV[16,29,48]. A similar change in the chemical state of elemental Cu is also observed in the $NTN_1C_1O$ sample after reduction at high temperatures, as shown in Fig. 3 (h). The $Cu^0$ (2p1/2) and $Cu^0$ (2p3/2) peaks are observed at 951.88 and 932.20 eV, respectively. According to reports in the literature, the electronic potential energy of alloys of transition metals can be sensitively changed[49,50]. In this work, some peaks of binding energy change by approximately 0.2 to 0.3 eV in the case of $Ni^0$ and $Cu^0$ in the $Ni_{0.5}Cu_{0.5}$ alloy. The $Ni^0$ and $Cu^0$ exist in the form of metallic alloy nanoparticles in the reduced sample, which further confirms the exsolution of metallic $Ni_{0.5}Cu_{0.5}$ alloy on the ceramic substrate. The XPS results further confirm the reversible transformation between the oxidised $NbTi_{0.5}(Ni_xCu_{1-x})_{0.5}O_4$ solid solution and the reduced $Nb_{1.33}Ti_{0.67}O_4$ ceramic electronic conductor loaded with metallic $Ni_xCu_{1-x}$ alloys.

TGA of the oxidised $NTN_1C_1O$ and NTNO samples was conducted from room temperature to 1000°C at a heating rate of 4°C·$min^{-1}$ in a reducing atmosphere of 5% $H_2$/Ar. To ensure sufficient reduction of the powder sample, the predetermined temperature at 1000°C is stabilised for as long as 3 h and then drifts to room temperature at the same rate, as previously stated. Fig. 4 (a) presents the percentage weight change of the oxidised NTNO powder as a function of temperature when heated under a 5% $H_2$/Ar atmosphere. The weight loss reaches 7.35% for the NTNO sample because of the loss of oxygen under such reducing conditions, which is in a good agreement with the chemical change of the $NbTi_{0.5}Ni_{0.5}O_4$ solid solution to the reduced Ni + $Nb_{1.33}Ti_{0.67}O_4$ composite material. In

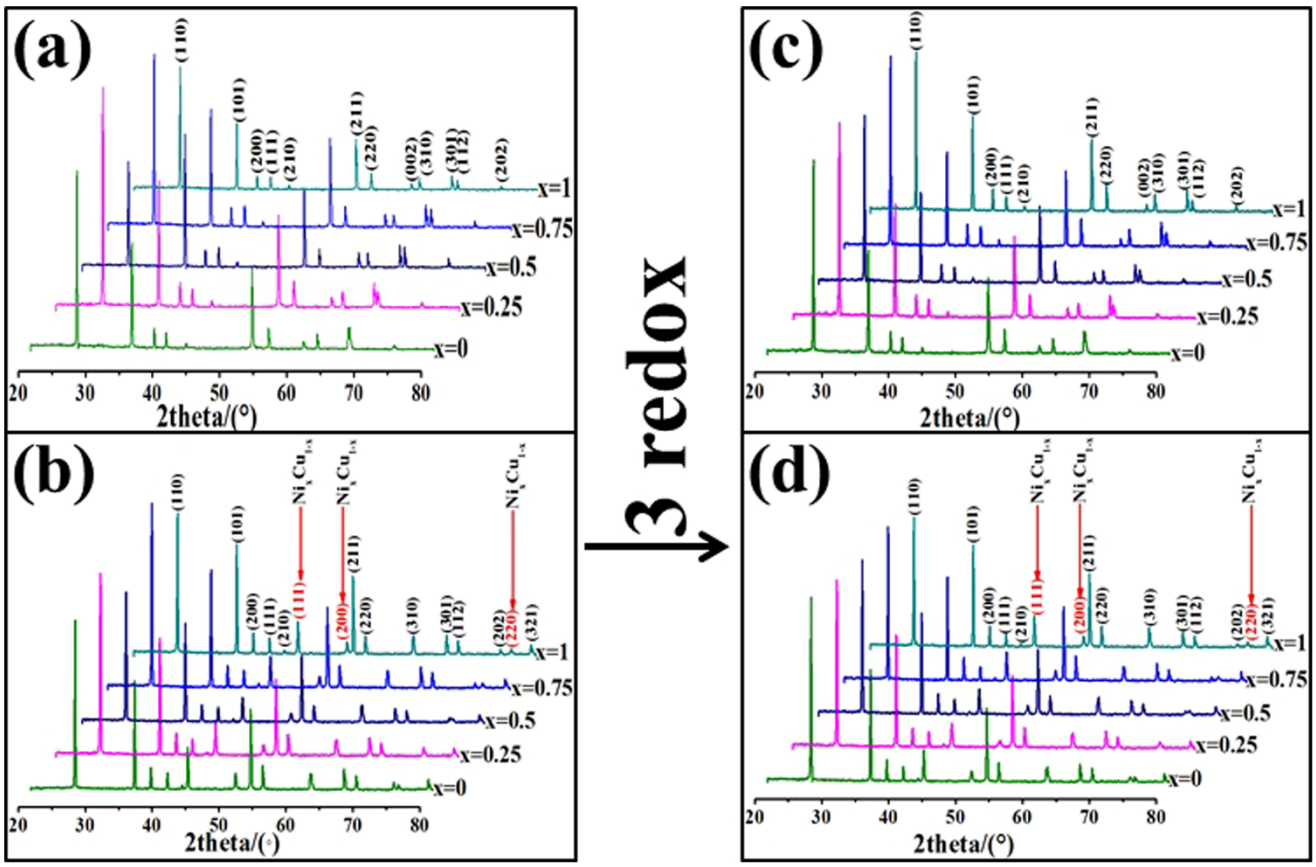


**Figure 1** | XRD patterns of $NbTi_{0.5}(Ni_xCu_{1-x})_{0.5}O_4$ (a: patterns of the oxidised form; b: patterns of the reduced form; c: patterns of oxidised form after three redox cycles; d: patterns of the reduced form after three redox cycles).

comparison, the weight loss of the studied $NTN_1C_1O$ powder reached approximately 7.59%, as seen in Fig. 4 (b), which is reasonably consistent with the theoretical value of 7.61% corresponding to the oxygen loss according to the chemical reaction presented in equation (1). Notably, the onset temperature of weight loss for the NTNO sample is approximately 750°C, as determined from the results in Fig. 4 (a), where the *in situ* exsolution of Ni metal is anticipated. Nevertheless, the weight loss of $NTN_1C_1O$ starts at temperatures as low as approximately 600°C to grow the metallic alloy. This growth may occur because the incorporation of copper reduces the chemical reaction barrier of metal exsolution and thus facilitates the reversible phase change to grow the metallic NiCu alloys. As evident in both Fig. 4 (a) and Fig. 4 (b), a small weight loss always occurred during the process of cooling. This weight loss is likely to exceed 7.40 and 7.61% for the NTNO and $NTN_1C_1O$, respectively, if the samples experience longer reduction times at higher temperatures. Ultimately, the obtained reduced sample may be oxygen-deficient $Nb_{1.33}Ti_{0.67}O_{4-\delta}$ + Ni or oxygen-deficient $Nb_{1.33}Ti_{0.67}O_{4-\delta}$ + $Ni_{0.5}Cu_{0.5}$. Despite the different proportions, our conclusion through reasoning is that these results coincide with the aforementioned results, as shown in Fig 3.

$$4NbTi_{0.5}(Ni_xCu_{1-x})O_4 + 4H_2 \rightarrow 2Ni_xCu_{1-x} + 3Nb_{1.33}Ti_{0.67}O_4 + 4H_2O \quad (1)$$

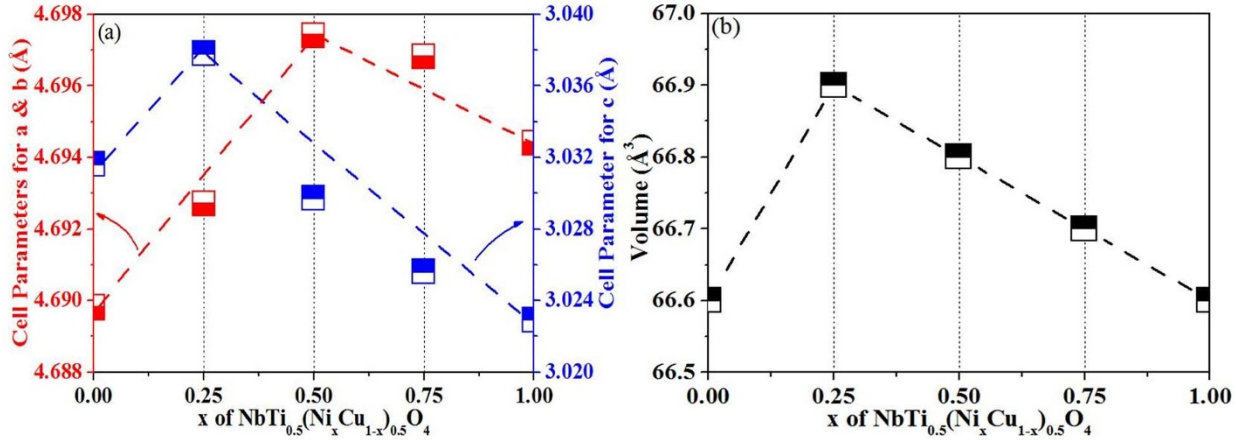


**Figure 2** | Cell parameters of the oxidised $NbTi_{0.5}Ni_xCu_{1-x}O_4$ powder samples with x = 0, 0.25, 0.5, 0.75 and 1.0.

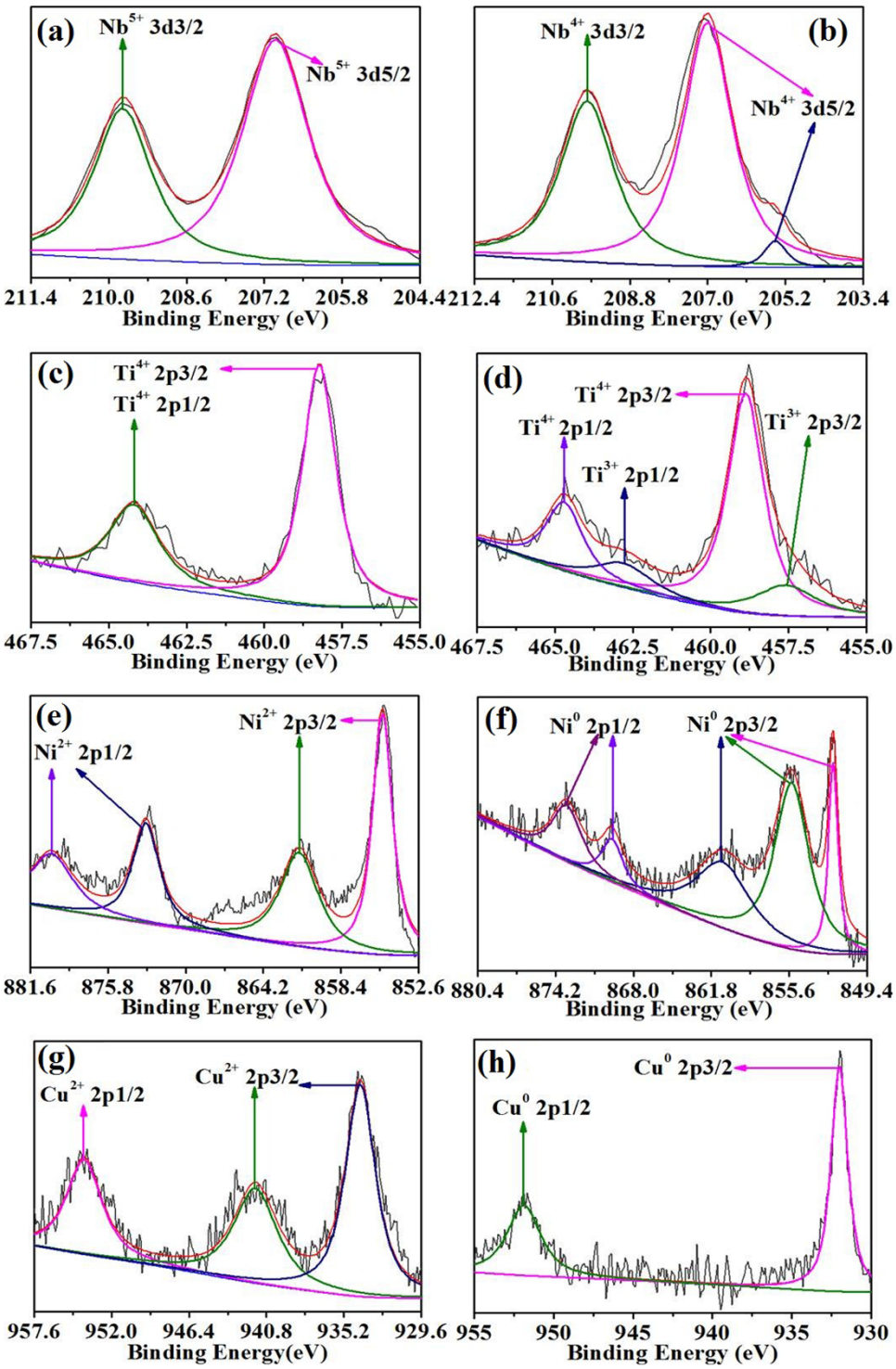


**Figure 3 | XPS results for Nb(a), Ti(c), Ni(e) and Cu(g) in the oxidised $NbTi_{0.5}(Ni_{0.75}Cu_{0.25})_{0.5}O_4$ and for Nb(b), Ti(d), Ni(f) and Cu(h) in the reduced $NbTi_{0.5}(Ni_{0.75}Cu_{0.25})_{0.5}O_4$.**

High-resolution transmission electron microscopy (HR-TEM) analysis of the oxidised $NTN_1C_1O$ reveals lattice spacings of 2.546 Å (101) and 3.322 Å (110), as shown in Figs. 5 (a) and (b), consistent with the separation spacing determined by the XRD analysis. As presented in Figs. 5 (c) and 5 (d), the corresponding lattice spacing of the parent material, $Nb_{1.33}Ti_{0.67}O_4$, can be obtained as 2.537 Å (101) and 3.363 Å (110). Moreover, the interplanar spacing is 2.238 Å (111). These spacings can be demonstrated by the results of the XRD analysis, shown in Figs. 1 and 2. Furthermore, the reduction of the $NTN_1C_1O$ leads to the growth of $Ni_{0.5}Cu_{0.5}$ alloy nanoparticles on the $Nb_{1.33}Ti_{0.67}O_4$ surfaces in Fig. 5 (d). The analysis results for the nickel copper alloy indicates a lattice spacing of 1.781 Å (200), consistent with the standard data for the alloy $Ni_1Cu_1$ data[51]. These TEM results further demonstrate and validate the reversible exsolution of metallic particles on the ceramic substrate through control of the phase transformation between the $NbTi_{0.5}(Ni_xCu_{1-x})O_4$ solid solution and $Ni_xCu_{1-x}/Nb_{1.33}Ti_{0.67}O_4$, as confirmed by the aforementioned XRD, XPS and TGA analyses. More importantly, the TEM results reveal that

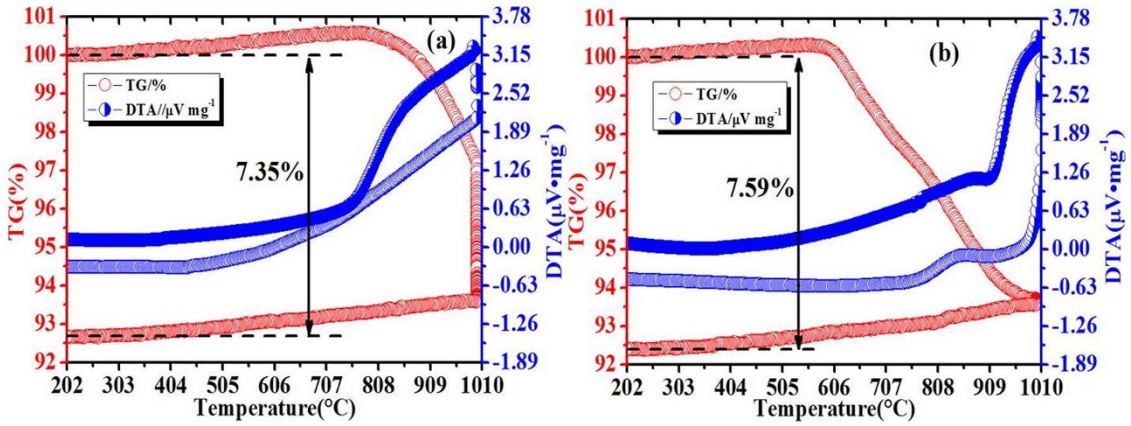


**Figure 4** | TGA thermograms of the oxidised form of $NbTi_{0.5}Ni_{0.5}O_4$ (a) and $NbTi_{0.5}Ni_{0.25}Cu_{0.25}O_4$ (b) in 5% $H_2$/Ar; the heating rate was 5°C $min^{-1}$.

the alloy particles are exsolved to *in situ* grow and anchor to the surface of the highly electronically conducting $Nb_{1.33}Ti_{0.67}O_4$ in the form of heterojunctions, which avoids any possible agglomeration of exsolved metallic nanoparticles on the substrate surface at high temperatures. The metal alloy nanoparticles can be re-incorporated or re-exsolved into/from the host material, yielding a catalyst that can be regenerated through periodic exposure of the material to oxidising/reducing conditions.

Fig. 6 shows the SEM and energy-dispersive X-ray spectroscopy (EDS) maps taken from the oxidised and reduced $NbTi_{0.5}(Ni_{0.5}Cu_{0.5})_{0.5}O_4$ pellets. The sintered samples were reduced in 5% $H_2$/Ar at 900°C for 17 h. As shown in Fig. 6 (a), the Ni and Cu are homogeneously dispersed in the oxidised $NTN_1C_1O$ sample and the other elements are also well distributed in the bulk. Although the oxidised sintered $NTN_1C_1O$ pellet is not highly dense, clear images are still observed for the sample with low sinterability and high porosity. In comparison, uniform exsolved nanoparticles anchor on the surface of the reduced $NbTi_{0.5}(Ni_{0.5}Cu_{0.5})_{0.5}O_4$ pellet, as shown in Fig. 6 (b), which is further confirmed by the EDS maps of the Ni and Cu. In addition, the Nb, Ti and O, which are components of the new phase of $Nb_{1.33}Ti_{0.67}O_4$, as previously discussed, are distributed evenly in the sample. The SEM and EDS results presented in Figure 6 (b) of the reduced $NTN_1C_1O$ suggest the exsolution of $Ni_{0.5}Cu_{0.5}$ alloy nanoparticles to anchor on the substrate surfaces. The presence of $Ni_{0.5}Cu_{0.5}$ alloy nanoparticles is further confirmed by the SEM and EDS results in addition to the XRD, XPS and TEM results, as previously mentioned. These results indicate that the reversible exsolution of NiCu alloy nanoparticles from the parent $NbTi_{0.5}(Ni_xCu_{1-x})_{0.5}O_4$ material to grow *in situ* and anchor the metal alloy nanocatalyst on the $Nb_{1.33}Ti_{0.67}O_4$ surface is successful. The dispersed $Ni_xCu_{1-x}$ nanoparticles anchoring on the $Nb_{1.33}Ti_{0.67}O_4$ surface are expected to prohibit the agglomeration and improve the electrocatalytic activity of the composite cathode for high-temperature $CO_2$ electrolysis.

The dependence of the conductivity of the samples on the temperature and oxygen partial pressure was systematically investigated, as shown in Fig. 7. According to the literature, $Nb_{1.33}Ti_{0.67}O_4$ is a mixed conductor because of the edge sharing of $NbO_6$ octahedra along the c-axis, which results in Nb-Nb metal bond overlap with an inter-metallic distance of 3 Å[29]. The reduced $NbTi_{0.5}(Ni_xCu_{1-x})_{0.5}O_4$ ceramic samples ($Nb_{1.33}Ti_{0.67}O_4$ + $Ni_xCu_{1-x}$) exhibit greater conductivity, as shown in Fig. 7 (a), because the metallic $Ni_xCu_{1-x}$ nanoparticles dispersed on the substrate improve the electrical conductivity under a reducing atmosphere (5% $H_2$/Ar, 99.99% purity). The reduced $NbTi_{0.5}Cu_{0.5}O_4$ ($Nb_{1.33}Ti_{0.67}O_4$ + Cu) sample exhibits the highest conductivity, which reaches approximately 500 $S \cdot cm^{-1}$ at 730°C. With increasing nickel composition, the conductivity of the reduced samples gradually decreases to

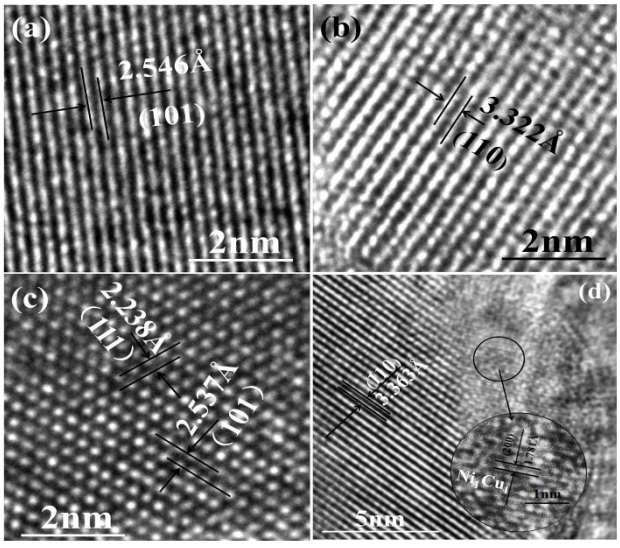


**Figure 5** | TEM results for the oxidised form of $NbTi_{0.5}Ni_{0.25}Cu_{0.25}O_4$ (a, b) and for the reduced form of $NbTi_{0.5}Ni_{0.25}Cu_{0.25}O_4$ (c, d).

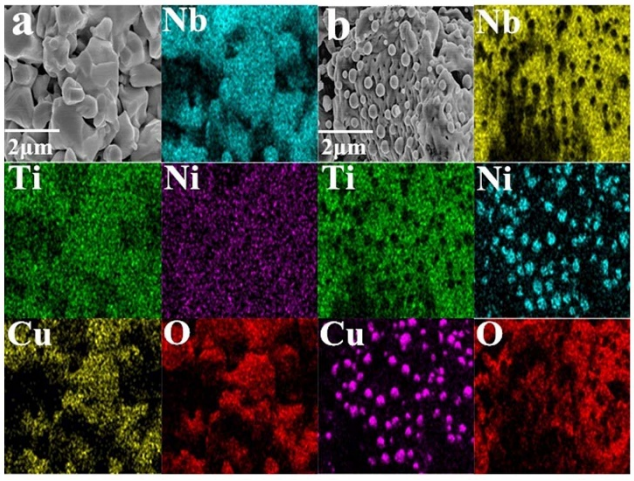


**Figure 6** | SEM and EDS results for the oxidised form of $NbTi_{0.5}Ni_{0.25}Cu_{0.25}O_4$ (a) and for the reduced form of $NbTi_{0.5}Ni_{0.25}Cu_{0.25}O_4$ (b).

204 $S \cdot cm^{-1}$ with the maximum Ni content in the reduced $NbTi_{0.5}Ni_{0.5}O_4$ ($Nb_{1.33}Ti_{0.67}O_4$ + Cu) at the same temperature. This phenomenon is possibly due to the Cu metal exhibiting conductivity superior to that of Ni metal at high temperatures. The conductivities measured under a reducing atmosphere is mainly attributed to the electronically conducting ceramic $Nb_{1.33}Ti_{0.67}O_4$, in agreement with results reported in the literature[26,27]; however, the percolating metal network is not formed due to the presence of dispersed $Ni_xCu_{1-x}$ alloys. As shown in Fig. 7 (b), the conductivities of $Nb_{1.33}Ti_{0.67}O4$ + $Ni_xCu_{1-x}$ are generally independent of the oxygen partial pressure at partial pressures less than $10^{-4}$ atm; however, the conductivity significantly decreases when the samples are oxidised at high oxygen partial pressure due to the oxidation of $Nb_{1.33}Ti_{0.67}O_4$ + $Ni_xCu_{1-x}$ to the $NbTi_{0.5}(Ni_xCu_{1-x})_{0.5}O_4$ solid solution.

Fig. 8 shows the AC impedance plots of the symmetric cells tested under a series of different hydrogen partial pressures (0, 2, 5, 20, 40, 50, 60, 80 and 100% $H_2$) with nitrogen to adjust the hydrogen concentrations at 800°C. The impedance plots show two intercepts with the real axis, where the series resistant of the cell ($R_s$) corresponds to the first intercept and the difference between the two intercepts is a measure of the electrode polarisation resistance ($R_p$). The Zview software (IM6, Zahner, Germany) was employed to calculate $R_s$ and $R_p$, as reported in our previous work[46,48]. The ionic resistance of the 1 mm YSZ electrolyte is the primary contributor to the $R_s$, which is approximately 2 Ω and is generally stable over a wide range of hydrogen partial pressures. In our previous work, we reported that a symmetric solid-oxide cell with a composite electrode based on $Nb_{1.33}Ti_{0.67}O_4$ exhibits poor performance, where the electrode polarisation resistance is approximately 300 Ω $cm^2$ [29]. As shown in Figs. 8 (a), (b) and (c), the $R_p$ of the symmetric cell based on NTNO-SDC decreases from 18.65 to 3.02 Ω $cm^2$ over the hydrogen partial pressure ranging of 0 to 100%. Similarly, the $R_p$ values of the symmetric cells based on $NTN_3C_1O$, $NTN_1C_1O$, $NTN_1C_3O$ and NTCO are shown in Figs. 8 (d, e, f), Figs. 8 (g, h, i), Figs. 8 (g, k, l), and Figs. 8 (m, n, o), respectively; the $R_p$ decreases from 34.72 to 6.08 Ω $cm^2$, 45.61 to 14.26 Ω $cm^2$, 57.04 to 7.64 Ω $cm^2$ and 39.85 Ω $cm^2$ to 10.81 Ω $cm^2$, respectively. All of the $R_p$ values change as functions of the hydrogen partial pressure, which suggests that the stronger reducing atmosphere improves the electrode polarisations. A stronger reducing atmosphere favours the growth of metallic $Ni_xCu_{1-x}$ alloy particles on the surface of the electrode skeleton and thus enhances the electrocatalytic activity of the composite electrodes. However, the polarisation resistance gradually decreases with increasing nickel content when compared with all of the proportions, which is attributed to the catalytic activity of nickel metal being greater than that of copper. The electrocatalytic activity of the composite electrode can be continuously tuned according to the strong dependence of the electrode activity on the alloy compositions under reducing atmospheres at high temperatures.

To investigate the sealing of the single solid-oxide electrolyser based on the $NTN_xC_{1-x}O$ composite cathode, we recorded the open-circuit voltage (OCV) with the cathode and anode exposed to 5% $H_2$/Ar and static air, respectively, and examined the separation between the anodic and cathodic gases. The OCVs of the cells reach approximately 1.0 V, which indicates good separation between the anodic and cathodic gases. Fig. 9 shows the I–V curve at 800°C with 100% $CO_2$ introduced to the cathode and with the anode exposed to static air. The relationship between the current and the applied voltage is far from linear, with the maximum current densities reaching 169.71, 113.17, 80.46, 69.14 and 56.57 mA $cm^{-2}$ at 1.6 V for the electrolysers based on NTNO, $NTN_3C_1O$, $NTN_1C_1O$, $NTN_1C_3O$ and NTCO, respectively. Numerous investigators have demonstrated that the electrolysis current depends on the availability of the three-phase interfaces. However, the electrolysis current also increases rapidly with increasing nickel content because of the high catalytic activity of nickel. Thus, a high content of nickel catalyst improves the cathode performance.

*In situ* AC impedance spectroscopy was carried out under different applied voltages to investigate the changes to $R_s$ and $R_p$, where $R_s$ and $R_p$ correspond to the series resistance and polarisation resistance of the electrolyser, respectively. As shown in Fig. 10, all of the series resistances, $R_s$, are stable; however, the $R_p$ values sharply decrease as a function of the applied voltage in the range of 1.2 to 1.4 V. The $R_p$ is significantly enhanced by the application of higher external potentials because the passing current density not only activates the electrode, but also electrochemically reduces the cathode to enhance the mixed conductivity and electrocatalytic activity. We observed that the $R_p$ is only 2.17 Ω·$cm^2$ at 1.4 V in $CO_2$ in the case of the NTNO cathode, whereas the $R_p$ is approximately 2.85 Ω·$cm^2$ at low voltage of 1.1 V as shown in Fig. 10 (a). However, as seen in Figs. 10 (b), (c) and (d), the $R_p$ values are 6.21, 9.94 and 6.22 Ω·$cm^2$ for the electrolysers with $NTN_3C_1O$, $NTN_1C_3O$ and NTCO cathodes at 1.4 V, respectively. Here, the exsolution of metallic nanoparticles may significantly improve the electrocatalytic activity of the composite cathodes, and the passing current may further activate the composite electrodes and improve the electrode polarisation. To a certain extent, we conclude that the nickel content in NiCu alloys and the crystal structure of NiCu alloys may have a coordinated action for $CO_2$ electrolysis; if this is not the case, the $R_p$ should increase with decreasing proportion of nickel because nickel exhibits superior catalytic performance for $CO_2$ decomposition.

Fig. 11 shows the rate of CO production and the current efficiency of the electrolysers *versus* the nickel composition based on

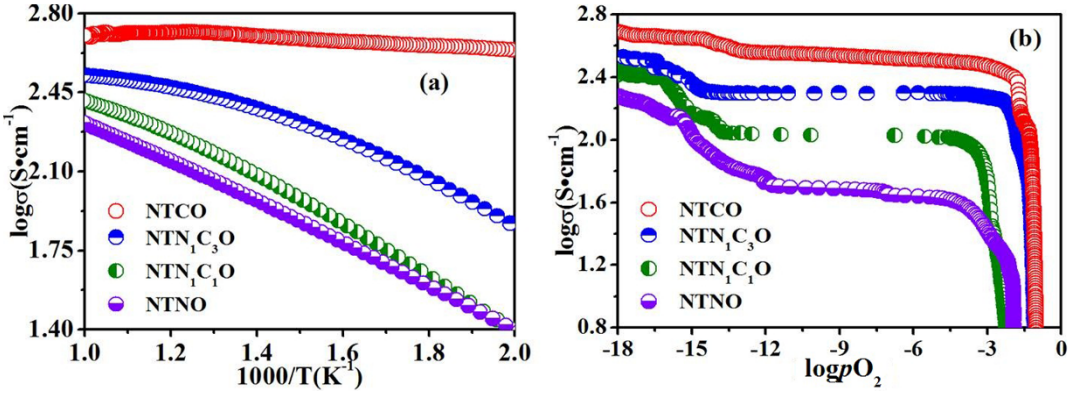


**Figure 7 | (a) The dependence of conductivity on temperature of the reduced form of $NbTi_{0.5}(Ni_xCu_{1-x})_{0.5}O_4$ (x = 0, 0.25, 0.5 and 1.0) samples; (b) the dependence of the conductivity on the oxygen partial pressure of the reduced form of $NbTi_{0.5}(Ni_xCu_{1-x})_{0.5}O_4$ (x = 0, 0.25, 0.5 and 1.0) samples at 800°C.**

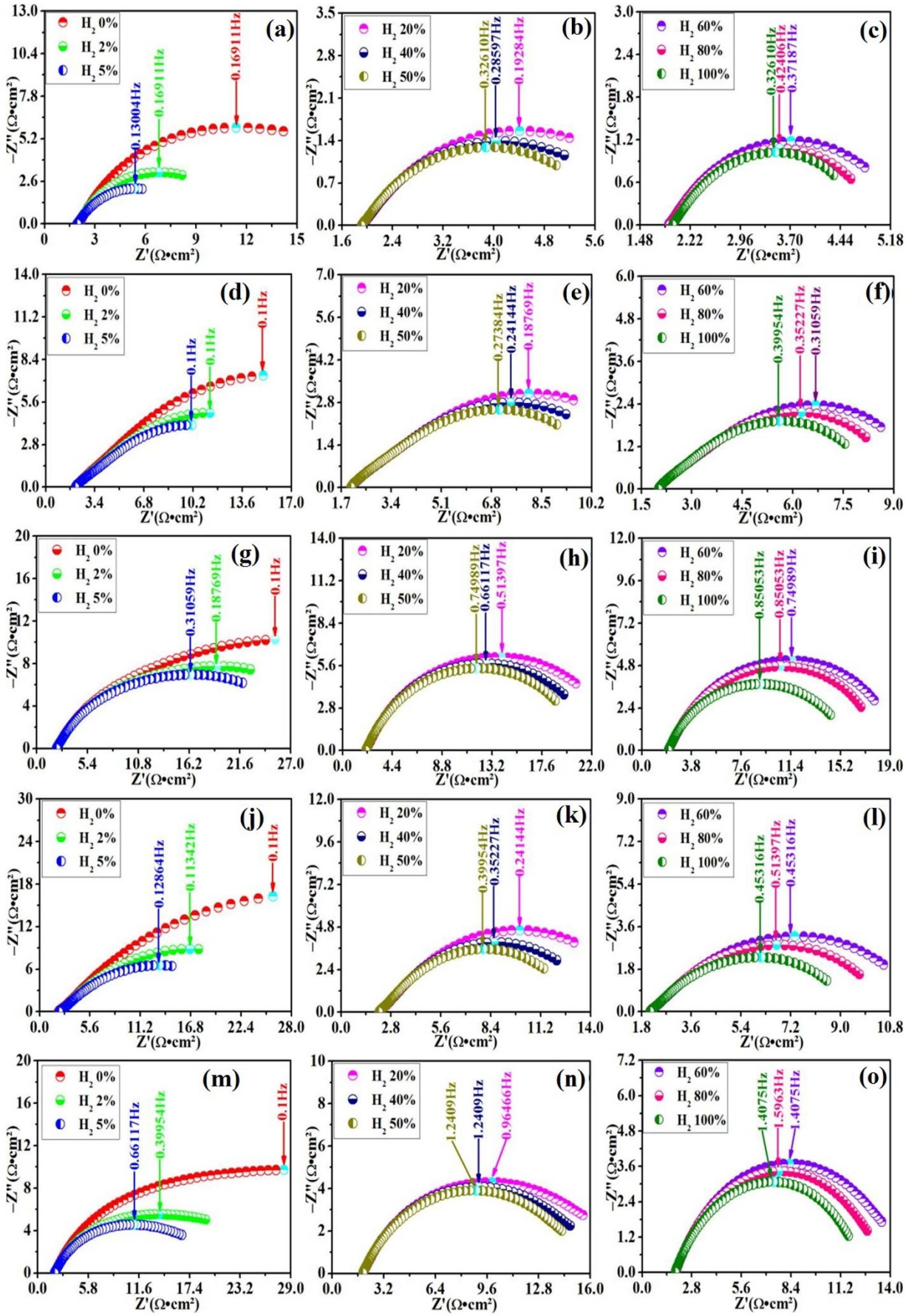


**Figure 8** | AC impendence plots for the symmetrical cells based on $NbTi_{0.5}(Ni_xCu_{1-x})_{0.5}O_4$ electrodes with x = 1 (a, b, c), x = 0.75 (d, e, f), x = 0.5, (g, h, i), x = 0.25 (j, k, l) and x = 0 (m, n, o) tested at 800 °C under different hydrogen partial pressures.

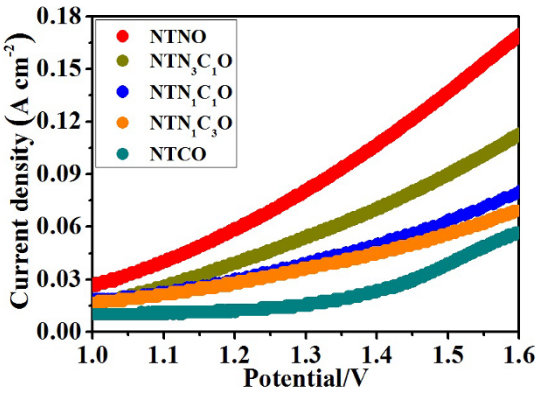


**Figure 9 | I–V curves of the solid oxide electrolysers based on $NbTi_{0.5}(Ni_xCu_{1-x})_{0.5}O_4$ (x = 0, 0.25, 0.5, 0.75 and 1.0) cathodes for $CO_2$ electrolysis at 800°C.**

$NTN_xC_{1-x}O$ composite cathodes for direct $CO_2$ electrolysis under applied voltages of 1.2, 1.3 and 1.4 V, respectively. As shown in Fig. 11 (a), the CO production rates gradually improve with increasing applied voltage for all of the electrolysers and exhibit the highest rates at a final applied voltage of 1.4 V because high voltages favour $CO_2$ splitting at the cathode. The CO production rate of the electrolyser with the $NTN_3C_1O$ (x = 0.75) composite cathode is 0.1629 ml·min$^{-1}$·cm$^{-2}$ at 1.4 V, which is approximately three times greater than the rate of 0.04113 ml·min$^{-1}$·cm$^{-2}$ for the cell at the same applied voltage of 1.2 V. However, we note that the productionrate of CO is strongly dependent on the nickel composition in the parent material, i.e., the $NbTi_{0.5}(Ni_xCu_{1-x})_{0.5}O_4$ solid solution, which definitely determines the nickel concentration of the metallic $Ni_xCu_{1-x}$ alloy nanocatalysts. The electrolyser produces CO at a rate of 0.07663 ml·min$^{-1}$·cm$^{-2}$ in the case of the NTCO composite cathode and was significantly enhanced to as high as 0.3866 ml·min$^{-1}$·cm$^{-2}$ in the case of the NTNO cathode at a voltage of 1.4 V. These results again verify the superior catalytic activity of the nickel catalyst toward electrochemical $CO_2$ splitting. Similar behaviour of the CO production rate *versus* the nickel composition was also observed at applied voltages of 1.2 and 1.3 V. Clearly, the CO production improves slowly when $x < 0.5$ and then increases rapidly in the interval of $0.5 \leq x \leq 1$. This behaviour can be attributed to the excellent catalytic activity of the $Ni_xCu_{1-x}$ alloy when the nickel concentration is high.

Fig. 11 (b) shows the current efficiencies of the electrolysers *versus* the nickel composition for the case of $NTN_xC_{1-x}O$ composite cathodes during direct $CO_2$ electrolysis under different applied voltages. The current efficiencies gradually improve with increasing copper content in the composition range of $0 \leq x \leq 0.75$ because of the adsorption of $CO_2$ onto copper. However, the current efficiencies begin to decrease when the copper content is in the rage of $0.75 \leq x \leq 1$, although they are still greater than the current efficiencies of the cathode with x = 0. Copper with excellent $CO_2$/CO adsorption properties is expected to facilitate the electrochemical conversion of $CO_2$ to CO and to therefore improve the current efficiencies. The optimum composition of $Ni_{0.75}Cu_{0.25}$ alloy catalyst combines the advantages of both metallic nickel and metallic copper to maximise current efficiencies for the direct $CO_2$ electrolysis. The highest current efficiency of 74.29% are obtained in the case of the $NTN_3C_1O$ cathode at 1.4 V. Similarly, the current efficiencies are accordingly improved *versus* the applied voltage because the applied voltages electrochemically reduce/activate the composite cathodes to enhance the electrocatalytic activity[56]. The *in situ* growth and anchoring of $Ni_xCu_{1-x}$ alloy nanocatalysts on the $Nb_{1.33}Ti_{0.67}O_4$ surface combines the advantages of metallic nickel and copper and produces a synergistic effect to maximise the current efficiencies for the direct electrolysis of $CO_2$. The coupling of metal catalysts with the electronically conducting ceramic substrate offers possibilities for the direct $CO_2$ electrolysis at high temperatures.

## Conclusion

In this work, the *in situ* growth of $Ni_xCu_{1-x}$ (x = 0, 0.25, 0.50, 0.75 and 1.0) alloy catalysts was achieved to anchor on the redox-reversible

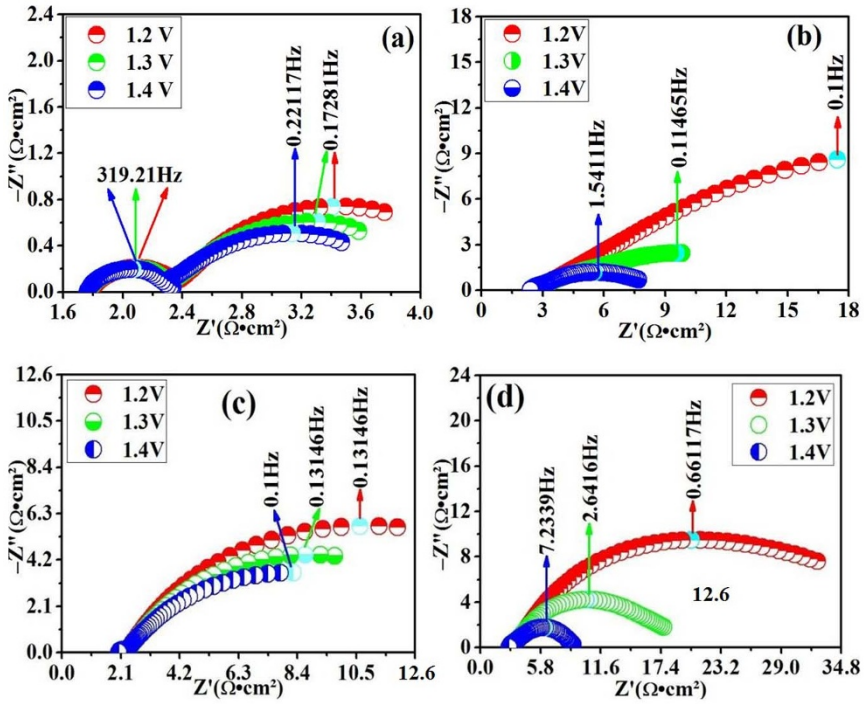


**Figure 10 | AC impendence plots of the solid oxide electrolysers based on $NbTi_{0.5}(Ni_xCu_{1-x})_{0.5}O_4$ (a: x = 1; b: x = 0.75; c: x = 0.25; d: x = 0) composite electrodes for $CO_2$ electrolysis with the oxygen electrode exposed in static air at 800°C.**

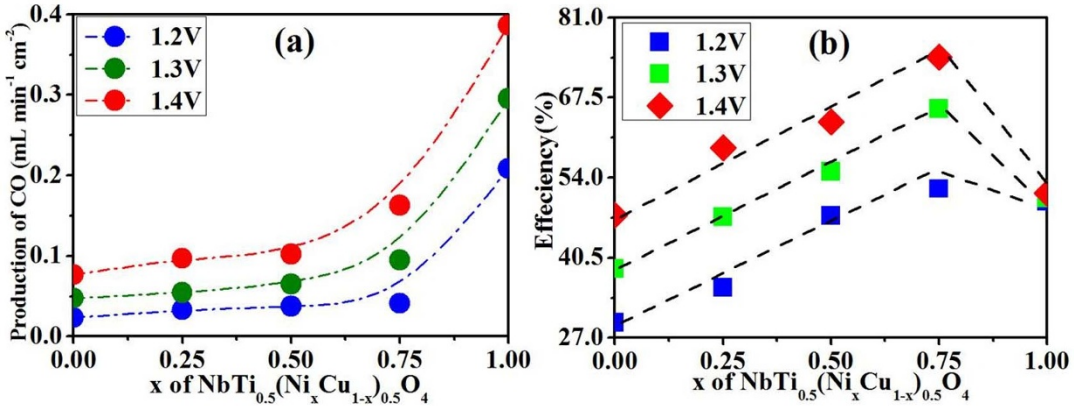


**Figure 11** | **(a) CO production rate for the cells based on $NbTi_{0.5}(Ni_xCu_{1-x})_{0.5}O_4$ (x = 0, 0.25, 0.5, 0.75 and 1.0) composite cathode *versus* x of $NbTi_{0.5}(Ni_xCu_{1-x})_{0.5}O_4$; (b) the relationship between the current efficiency of the $CO_2$ electrolysis and x in the $NbTi_{0.5}(Ni_xCu_{1-x})_{0.5}O_4$ (x = 0, 0.25, 0.5, 0.75 and 1.0) composite cathodes.**

$Nb_{1.33}Ti_{0.67}O_4$ ceramic substrate in the form of heterojunctions. The exsolution/dissolution of the metal particles is completely reversible during redox cycling. The electrocatalytic activity of the composite electrode based on $Ni_xCu_{1-x}/Nb_{1.33}Ti_{0.67}O_4$ can be continuously tuned by tailoring the alloy composition. The coupling of metal catalyst with the electronically conducting ceramic substrate achieves direct $CO_2$ electrolysis at high temperatures, whereas the combined advantages of metallic nickel and copper produces a synergistic effect to maximise the current efficiencies. Electrocatalytic activity of the composite materials was achieved through direct exsolution of metal particles from the crystal lattice of the ceramic oxides under a reducing atmosphere at higher temperatures. The current work expands our understanding of advanced ceramic cathodes with excellent electrocatalytic activity in the field of high-temperature electrolysis.


1. Ge, X. M., Chan, S. H., Liu, Q. L. & Sun, Q. Solid Oxide Fuel Cell Anode Materials for Direct Hydrocarbon Utilization. *Adv. Energy Mater.* **2**, 1156–1181 (2012).
2. Ishihara, T., Jirathiwathanakul, N. & Zhong, H. Intermediate temperature solid oxide electrolysis cell using $LaGaO_3$ based perovskite electrolyte. *Energy Environ. Sci.* **3**, 665–672 (2010).
3. Lan, R., Irvine, J. T. S. & Tao, S. W. Ammonia and related chemicals as potential indirect hydrogen storage materials. *Int. J. Hydrogen Energy* **37**, 1482–1497 (2012).
4. Sridhar, K. R. & Vaniman, B. T. Oxygen production on Mars using solid oxide electrolysis. *Solid State Ionics* **93**, 321–328 (1997).
5. Qi, W. T. *et al.* Remarkable chemical adsorption of manganese-doped titanate for direct carbon dioxide electrolysis. *J. Mater. Chem. A* **2**, 6904–6915 (2014).
6. Pihlatie, M., Kaiser, A. & Mogensen, M. Redox stability of SOFC: thermal analysis of Ni-YSZ composites. *Solid State Ionics* **180**, 1100–1112 (2009).
7. Tao, S. W. & Irvine, J. T. S. A redox-stable efficient anode for solid-oxide fuel cells. *Nat. Mater.* **2**, 320–323 (2003).
8. Bidrawn, F. *et al.* Efficient reduction of $CO_2$ in a solid oxide electrolyzer. *Electrochem. Solid St.* **11**, B167–B170 (2008).
9. Ebbesen, S. D. & Mogensen, M. Electrolysis of carbon dioxide in solid oxide electrolysis cells. *J. Power Sources* **193**, 349–358 (2009).
10. Katsutoshi, N., Kulathuiyer, S., Kenichi, A. & Johannes, A. L. Carbon Deposition during Carbon Dioxide Reforming of Methane-Comparison between $Pt/Al_2O_3$ and $Pt/ZrO_2$. *J. Catal* **197**, 34–42 (2001).
11. Tucker, M. C. *et al.* Cu-YSZ cermet solid oxide fuel cell anode prepared by high-temperature sintering. *J. Power Sources* **195**, 3119–3123 (2010).
12. Zhan, Z. L. & Lee, S. I. Thin film solid oxide fuel cells with copper cermet anodes. *J. Power Sources* **195**, 3494–3497 (2010).
13. Yang, X. D. & Irvine, J. T. S. $(La_{0.75}Sr_{0.25})_{0.95}Mn_{0.5}Cr_{0.5}O_3$ as the cathode of solid oxide electrolysis cells for high temperature hydrogen production from steam. *J. Mater. Chem.* **18**, 2349–2354 (2008).
14. Xu, S. S. *et al.* Direct electrolysis of $CO_2$ using an oxygen-ion conducting solid oxide electrolyzer based on $La_{0.75}Sr_{0.25}Cr_{0.5}Mn_{0.5}O_{3-\delta}$ electrode. *J. Power Sources* **230**, 115–121 (2013).
15. Li, Y. X. *et al.* Composite fuel electrode $La_{0.2}Sr_{0.8}TiO_{3-\delta}$-$Ce_{0.8}Sm_{0.2}O_{2-\delta}$for electrolysis of $CO_2$ in an oxygen-ion conducting solid oxide electrolyser. *Phys. Chem. Chem. Phys.* **14**, 15547–15553 (2012).
16. Gan, Y. *et al.* Composite cathode $La_{0.4}Sr_{0.4}TiO_{3-\delta}$-$Ce_{0.8}Sm_{0.2}O_{2-\delta}$ impregnated with Ni for high-temperature steam electrolysis. *J. Power Sources* **245**, 245–255 (2014).
17. Li, S. S., Li, Y. X., Gan, Y. & Xie, K. Electrolysis of $H_2O$ and $CO_2$ in an oxygen-ion conducting solid oxide electrolyzer with a $La_{0.2}Sr_{0.8}TiO_{3+\delta}$ composite cathode. *J. Power Sources* **218**, 244–249 (2012).
18. Bossche, M. & McIntosh, S. Pulse reactor studies to assess the potential of $La_{0.75}Sr_{0.25}Cr_{0.5}Mn_{0.4}X_{0.1}O_{3-\delta}$ (X = Co, Fe, Mn, Ni, V) as direct hydrocarbon solid oxide fuel cell anodes. *Chem. Mater.* **22**, 5856–5865 (2010).
19. Ghosh, A., Azad, A. K. & Irvine, J. T. S. Study of Ga Doped LSCM as an Anode for SOFC. *ECS Transactions* **35**, 1337–1343 (2011).
20. Lay, E., Gauthiera, G. & Dessemond, L. Preliminary studies of the new Ce-doped La/Sr chromo-manganite series as potential SOFC anode or SOEC cathode materials. *Solid State Ionics* **189**, 91–99 (2011).
21. Kim, G. *et al.* Investigation of the structural and catalytic requirements for high-performance SOFC anodes formed by infiltration of LSCM. *Electrochem. Solid St.* **12**, B48–B52 (2009).
22. Tucker, M. C. *et al.* Performance of metal-supported SOFCs with infiltrated electrodes. *J. Power Sources* **171**, 477–482 (2007).
23. Xu, S. S. *et al.* Composite cathode based on Fe-loaded LSCM for steam electrolysis in an oxide-ion-conducting solid oxide electrolyser. *J. Power Sources* **239**, 332–340 (2013).
24. Li, Y. X. *et al.* Composite cathode based on Ni-loaded $La_{0.75}Sr_{0.25}Cr_{0.5}Mn_{0.5}O_{3-\delta}$ for direct steam electrolysis in an oxide-ion-conducting solid oxide electrolyzer. *Int. J. Hydrogen Energy* **38**, 10196–10207 (2013).
25. Neagu, D. *et al.* In situ growth of nanoparticles through control of non-stoichiometry. *Nat. Chem* **5**, 916–923 (2013).
26. Boulfrad, S., Cassidy, M. & Irvine, J. T. S. $NbTi_{0.5}Ni_{0.5}O_4$ as anode compound material for SOFCs. *Solid State Ionics* **197**, 37–41 (2011).
27. Lashtabeg, A., Irvine, J. T. S. & Feighery, A. Thermomechanical and conductivity studies of doped niobium titanates as possible current collector material in the SOFC anode. *Ionics* **9**, 220–226 (2003).
28. Lashtabeg, A., Vazquez, J. C., Irvine, J. T. S. & Bradley, J. L. StructureConductivityand Thermal Expansion Studies of Redox Stable Rutile Niobium Chromium Titanates in Oxidizing and Reducing Conditions. *Chem. Mater.* **21**, 3549–3561 (2009).
29. Li, S. S. *et al.* High-performance fuel electrodes based on $NbTi_{0.5}M_{0.5}O_4$ (M = Ni, Cu) with reversible exsolution of the nano-catalyst for steam electrolysis. *J. Mater. Chem. A* **1**, 8984–8993 (2013).
30. Meng, X. X. *et al.* Carbon-resistant Ni-YSZ/Cu-$CeO_2$-YSZ dual-layer hollow fiber anode for micro tubular solid oxide fuel cell. *Int. J. Hydrogen Energy* **8**, 3879–3886 (2014).
31. Meng, X. X. *et al.* Effect of the co-spun anode functional layer on the performance of the direct-methane microtubular solid oxide fuel cells. *J. Power Sources* **247**, 587–593 (2014).
32. Ye, X. F. *et al.* Application of a Cu-$CeO_2$/Ni-yttria-stabilized zirconia multi-layer anode for anode-supported Solid Oxide Fuel Cells operating on $H_2$-CO. *J. Power Sources* **13**, 5499–5502 (2011).
33. Fuerte, A., Valenzuela, R. X., Escudero, M. J. & Daza, L. Effect of cobalt incorporation in copper-ceria based anodes for hydrocarbon utilisation in Intermediate Temperature Solid Oxide Fuel Cells. *J. Power Sources* **196**, 4324–4331 (2011).
34. Pan, Y. X., Liu, C. J. & Shi, P. Preparation and characterization of coke resistant Ni/$SiO_2$ catalyst for carbon dioxide reforming of methane. *J. Power Sources* **176**, 46–53 (2008).
35. Thomaz Augusto Guisard, R. & Sonia Regina Homem, M. Sintering studies on Ni-Cu-YSZ SOFC anode cermet processed by mechanical alloying. *J. Therm. Anal. Calorim* **97**, 775–780 (2009).
36. Thomaz Augusto Guisard, R. & Sonia Regina Homem, M. Microstructure design by mechanical alloying. *J. Eur. Ceram. Soc.* **30**, 2991–2996 (2010).

37. Thomaz Augusto Guisard, R. & Sonia Regina Homem, M. Cu-Ni-YSZ anodes for solid oxide fuel cell by mechanical alloying processing. *Int. J. Mater. Res.* **101**, 128–132 (2010).
38. Islam, S. & Hill, J. M. Preparation of Cu-Ni/YSZ solid oxide fuel cell anodes using microwave irradiation. *J. Power Sources* **196**, 5091–5094 (2011).
39. Smirnov, A. A. *et al.* Effect of the Ni/Cu ratio on the composition and catalytic properties of nickel-copper alloy in anisole hydrodeoxygenation. *Kinet. Catal.* **55**, 69–78 (2014).
40. Kim, J. Y. *et al.* Aqueous phase reforming of glycerol over nanosize Cu-Ni catalysts. *J. Nanosci. Nanotechno.* **13**, 593–597 (2013).
41. Liu, H. Y. *et al.* Insight into $CH_4$ dissociation on NiCu catalyst: A first-principles study. *Appl. Surf. Sci.* **258**, 8177–8184 (2012).
42. Khzouz, M., Wood, J., Pollet, B. & Bujalski, W. Characterization and activity test of commercial Ni/$Al_2O_3$, Cu/ZnO/$Al_2O_3$ and prepared Ni-Cu/$Al_2O_3$ catalysts for hydrogen production from methane and methanol. *Int. J. Hydrogen Energy* **38**, 1664–1675 (2013).
43. Vesselli, E. *et al.* Steering the chemistry of carbon oxides on a NiCu catalyst. *ACS Catal.* **3**, 1555–1559 (2013).
44. Gan, L. Y. *et al.* Catalytic Reactivity of CuNi Alloys toward $H_2O$ and CO Dissociation for an Efficient Water-Gas Shift: A DFT Study. *J. Phys. Chem. C* **116**, 745–752 (2012).
45. Gan, L. Y. & Zhao, Y. J. Inverse $NiO_{1-x}$/Cu Catalyst with High Activity toward Water-Gas Shift. *J. Phys. Chem. C* **116**, 16089–16092 (2012).
46. Li, Y. X. *et al.* Remarkable chemical adsorption of manganese-doped titanate for direct carbon dioxide electrolysis. *ACS Appl. Mater. Interfaces* **5**, 8553–8562 (2013).
47. Tao, S. W. & Irvine, J. T. S. Synthesis and Characterization of $(La_{0.75}Sr_{0.25})Cr_{0.5}Mn_{0.5}O_{3-\delta}$,a Redox-Stable, Efficient Perovskite Anode for SOFCs. *J. Electrochem. Soc.* **151**, A252–A259 (2004).
48. Xu, S. S. *et al.* Perovskite chromates cathode with resolved and anchored nickel nano-particles for direct high-temperature steam electrolysis. *J. Power Sources* **246**, 346–355 (2014).
49. Barbieri, P. F. *et al.* XPS and XAES study of Ag-Pd and Cu-Ni alloys: spectra, shifts and electronic structure information. *J. Electron. Spectrosc.* **135**, 113–118 (2004).
50. Naghash, A. R., Etsell, T. H. & Xu, S. XRD and XPS study of Cu-Ni interactions on reduced copper-nickel-aluminum oxide solid solution catalysts. *Chem. Mater.* **18**, 2480–2488 (2006).
51. Ngamlerdpokin, K. & Tantavichet, N. Electrodeposition of nickel-copper alloys to use as a cathode for hydrogen evolution in an alkaline media. *Int. J. Hydrogen Energy* **39**, 2505–2515 (2014).
52. Ahmed, B. *et al.* Development of novel LSM/GDC composite and electrochemical characterization of LSM/GDC based cathode-supported direct carbon fuel cells. *J. Solid State Electr.* **18**, 435–443 (2014).
53. Mori, T. *et al.* Influence of particle morphology on nanostructural feature and conducting property in Sm-doped $CeO_2$ sintered body. *Solid State Ionics* **30**, 641–649 (2004).
54. Xie, K. *et al.* A simple and easy one-step fabrication of thin $BaZr_{0.1}Ce_{0.7}Y_{0.2}O_{3-\delta}$ electrolyte membrane for solid oxide fuel cells. *J. Membrane Sci.* **325**, 6–10 (2008).
55. Wang, S. L. *et al.* Cost-effective tubular cordierite micro-filtration membranes processed by co-sintering. *J. Alloy. Compd.* **468**, 499–504 (2009).
56. Geetha, N. & Vinod, M. J. Modeling $CO_2$ electrolysis in solid oxide electrolysis cell. *J Solid State Electrochem.* **17**, 2361–2370 (2013).


## Acknowledgments

This work was financially supported by the Natural Science Foundation of China (NSFC), No. 21303037, the China Postdoctoral Science Foundation, No. 2013M53150, the Ministry of Education of Overseas Returnees Fund, No. 20131792, and the Fundamental Research Funds for the Central Universities, No. 2012HGZY0001.

## Author contributions

H.W. conducted the experiments. K.X., H.W., Y.Z., J.Y., J.C., Y.W. Y.Q. and J.Z. drafted the manuscript. K.X. and Y.W. supervised the experiments. All authors were involved in the data analysis and discussions.

## Additional information

**Supplementary information** accompanies this paper at http://www.nature.com/scientificreports

**Competing financial interests**: The authors declare no competing financial interests.

**How to cite this article:** Wei, H.S. *et al. In situ* Growth of $Ni_xCu_{1-x}$ Alloy Nanocatalysts on Redox-reversible Rutile (Nb,Ti)$O_4$ Towards High-Temperature Carbon Dioxide Electrolysis. *Sci. Rep.* **4**, 5156; DOI:10.1038/srep05156 (2014).